Calcium-Magnesium-Aluminosilicate (CMAS) corrosion resistance of high entropy rareearth phosphate ($Lu_{0.2}Yb_{0.2}Er_{0.2}Y_{0.2}Gd_{0.2}$)PO₄: A novel environmental barrier coating candidate

Keith Bryce¹, Yueh-Ting Shih², Liping Huang,² Jie Lian^{1,2*}

¹Department of Mechanical, Aerospace and Nuclear Engineering, Rensselaer Polytechnic Institute, NY 12180, USA

²Department of Materials Science & Engineering, Rensselaer Polytechnic Institute, NY 12180, USA

*Corresponding author, Email: lianj@rpi.edu

Abstract

Single phase (Lu_{0.2}Yb_{0.2}Er_{0.2}Y_{0.2}Gd_{0.2})PO₄ was synthesized, and its thermal properties and CMAS resistance were investigated to explore its potential as an environmental barrier coating (EBC) candidate. The high entropy phosphate (Lu_{0.2}Yb_{0.2}Er_{0.2}Y_{0.2}Gd_{0.2})PO₄ displays a lower thermal conductivity (2.86 W m⁻¹ K⁻¹ at 1250 K) than all the single component xenotime phase rare-earth phosphates. Interaction of (Lu_{0.2}Yb_{0.2}Er_{0.2}Y_{0.2}Gd_{0.2})PO₄ pellets with CMAS at 1300 °C led to the formation of a dense and uniformed Ca₈MgRE(PO₄)₇ reaction layer, which halted the CMAS penetration into the bulk pellet. At 1400 and 1500 °C the (Lu_{0.2}Yb_{0.2}Er_{0.2}Y_{0.2}Gd_{0.2})PO₄-CMAS corrosion showed CMAS penetrating beyond the reaction layer into the bulk pellet via the grain boundaries, and SiO₂ precipitates remaining at the pellet surface. The effects of duration, temperature, and compositions on the resistance against CMAS corrosion are discussed within the context of optimizing materials design and performance of high entropy rare-earth phosphates as candidates for advanced EBC applications.

1. Introduction

As aerospace vehicles are constantly improving in performance and fuel efficiency, engine sections and structural thermal protection systems will be operated at higher temperatures, hence more specialized materials are required for their development [1, 2]. In the past nickel-based superalloys in conjunction with cooling channels have been used in engine hot

sections, but as operating temperatures increase and approach the melting temperatures of these alloys, alternative materials have been proposed [3, 4]. One such group of materials is ceramic matrix composites (CMCs), which are comprised of a SiC matrix reinforced with woven SiC/carbon fibers and have already been used in stationary components of commercial aircraft engines as well as in gas turbines used for power generation [5]. CMCs, being made of SiC, are susceptible to water vapor oxidation at elevated temperatures in high-velocity gas stream conditions. Thus, they are used along with an environmental barrier coating (EBC) on their exposed surface to improve their oxidation resistance. However, potential EBC materials must function well to fulfill several key requirements. Firstly, EBCs should have a similar coefficient of thermal expansion (CTE) to CMCs to avoid delamination and cracking. They should also maintain a stable phase upon thermal cycling to avoid any volumetric changes that could aid in the delamination of the coating [6]. Next, they must be dense enough to prevent contact between the high-velocity gas stream and the CMC substrate and be resistant to chemical reactions with water vapor and molten CMAS, so as not to form any new reaction products that could cause delamination of the coating [7]. Based on these requirements, several materials have been proposed for EBC application such as (aluminates, mono-silicate, disilicates, and phosphates) but by far the most studied materials for EBC application are rare earth disilicates [8, 9, 10]. Rare earth disilicates have CTEs close to that of SiC, high melting points (>1750 °C), strong oxidation resistance, and relatively low thermal conductivity [11]. However, rare earth disilicates are highly susceptible to corrosion from molten CMAS at temperatures above 1200 °C.

CMASs are particulates from dust, sand, volcanic ash, fly ash, and runway debris that are ingested by the turbine as it intakes air. These particulates can clog cooling channels and cause mechanical damage to various engine components [12]. While CMASs are generally a mixture of calcium, magnesium, aluminum, and silica in various proportions depending on their environment of origin, they may also contain other metals such as iron, sodium, potassium, and titanium, usually in smaller amounts [13]. When these CMAS particulates come in contact with the hot sections of the turbine engine they melt and form a glassy silicate deposit on the surface of the EBC [14]. In the case of rare earth disilicates, the thermochemical interaction with CMAS melts generally occurs in one of two ways, depending on the rare earth disilicate in question. Firstly, the CMAS can react with the EBC, generating crystalline precipitates with different mechanical and thermodynamic properties than the original EBC. In the case of γ-Y2Si2O7, a Y-

Ca-Si apatite precipitate forms a layer between the disilicate and CMAS, which decreases the penetration of CMAS into the EBC [5]. Secondly, the CMAS melt interacts with the EBC by dissolution along the grain boundaries and pores in the EBC with little to no reaction. This causes a dilatation gradient within the EBC, and at high temperatures (>1500 °C) eventually leads to a built-up compressive stress in the top layer of the EBC and the formation of blister cracks [7]. Several methods have been used to improve EBC resistance to CMAS attacks, Turcer et al. (2018) eliminated CMAS-induced blister cracks from a dense β-Yb₂Si₂O₇ pellet, by combining a small amount of CMAS (1 vol%) in the Yb₂Si₂O₇ powder before sintering to increase the rate of penetration of the CMAS melt, thereby reducing the dilation gradient and increasing the creep relaxation to eliminate the blister cracks [7]. While this method eliminates blister cracks in the EBC, there are still some concerns with increasing the speed of the CMAS penetration into the EBC such as the CMAS melt dissolving through the EBC and reaching the SiC underneath even faster than usual. Wiesner et al. obtained similar results for their study of β-Yb₂Si₂O₇ interactions with CMAS at 1200-1500 °C, and they also observed the dissolution of the CMAS melt along the grain boundaries in the EBC without the precipitation of any other major phases [15]. However, the cracks were still observed due to a combination of shrinkage and swelling within the EBC microstructure rather than a dilation gradient.

The effects of CMAS corrosion have been studied for other potential EBC candidates. For example, Grant et al. (2010) investigated the interaction of molten CMAS with yttrium monosilicate and observed the reprecipitation of Ca₂Y₈(SiO₄)₆O₂ oxyapatite, in the form of a continuous reaction layer acting as a weak diffusion barrier between CMAS melt and the bulk pellet [16]. In a separate study, Turcer et al. (2018) investigated the performance of YAlO₃ as an EBC. Due to its high Y content, YAlO₃ reacted very quickly with the CMAS forming a protective layer of Y-Ca-Si apatite. The reaction zone is smaller than that of Y₂Si₂O₇, however, the mismatch of CTE between YAlO₃ and SiC remains a concern [5].

Rare earth phosphates were first proposed as candidates for EBC over a decade ago but have been given more attention lately. A study by Han et al. (2020) highlighted the thermal and mechanical properties of xenotime phase rare earth phosphates [17]. Particularly, xenotime phase rare earth phosphates display high phase stability at temperatures above 1500 °C, close CTE match with SiC, resistance to high-temperature water vapor corrosion, and relatively low thermal

conductivity. Hu et al. (2020) have also investigated rare earth phosphates for EBC applications. Specifically, LuPO₄ showed promising resistance to CMAS interaction, where it reacted with CMAS to form a layer of Ca₈MgLu(PO₄)₇ that halted CMAS penetration at 1300 °C even after 45 hours without the material experiencing any significant cracking or swelling as compared to rare earth disilicates [18]. Ridley et al. (2022) carried out a similar study but instead investigated the performance of YbPO₄ when corroded with CMAS of the same composition as in the study by Hu et al. (2020), at 1300 °C and up to 96 hours [19]. They reported improved CMAS corrosion resistance compared to ytterbium disilicate with the formation of a similar Ca₈MgYb(PO₄)₇ layer that halted CMAS penetration into the bulk pellet, and the formation of Yb₂Si₂O₇ precipitates within the CMAS at longer durations, which was attributed to the depletion of Ca and the enrichment of Yb and Si within the CMAS.

In the last several years, there has been great interest amongst the ceramic community in high-entropy ceramics (HEC), which are typically defined as ceramic compounds with a composition of five or more principal cations in equimolar fractions. The Gibbs free energy ΔG offers a method to determine the thermodynamic stability of these complex ceramics through ΔG_{mix} , which can be expressed as:

$$\Delta G_{\text{mix}} = \Delta H_{\text{mix}} - T \Delta S_{\text{mix}} \tag{1}$$

where ΔH_{mix} is the mixing enthalpy of the compound, T is the temperature and ΔS_{mix} is the mixing configurational entropy which can further be expressed by equation 2

$$\Delta S_{\text{mix}} = -nR \sum_{i=1}^{N} x_i \ln x_i$$
 (2)

where n is the molar ratio of the principal cations, R is the ideal gas constant, N is the number of element species in the principal cation sublattice and x_i is the molar fraction of the constituent i relative to the total constituents at the principal cation sublattice [20]. The gain in formation enthalpy decreases with the number of species added and is eventually surpassed by the monotonic increase in entropy gain. Once this occurs, the compound is entropy stabilized [21]. This entropy stabilization is caused by the increase in mass and size disorder of the mixed principal cations and has been shown to lower thermal conductivity, increase elastic modulus and act as an impedance to the diffusion in several materials [22, 23, 24, 25]. Y. Dong et al. (2019)

have already developed a single monoclinic phase high entropy rare earth disilicate with five components on the cation sublattice, which shows good phase stability up to 1300 °C, and a CTE close to that of SiC CMC, along with good corrosion resistance in a 50% H₂O–50% O₂ water-vapor environment at 1250 °C for 300 hours when coated on C_f/SiC composites [26].

In this work, we explored the potential of synthesizing a xenotime-based multicomponent rare-earth phosphate and evaluated its potential as an innovative material for EBC applications. Single phase high entropy rare-earth phosphate in a chemical formula of (Lu_{0.2}Yb_{0.2}Er_{0.2}Y_{0.2}Gd_{0.2})PO₄ was synthesized via the chemical precipitation method, and its structure, CTE, thermal stability, and thermal conductivity were characterized. The CMAS resistance of (Lu_{0.2}Yb_{0.2}Er_{0.2}Y_{0.2}Gd_{0.2})PO₄ was investigated at 1300 °C for durations of 5, 25, and 45 hours, then at 1400 and 1500 °C for 5 hours. Post-reaction characterization was carried out to analyze the reaction products and mechanisms.

2. Materials and Method

2.1 $(Lu_{0.2}Yb_{0.2}Er_{0.2}Y_{0.2}Gd_{0.2})PO_4$ Powder Synthesis

The rare earth phosphate powders (Lu_{0.2}Yb_{0.2}Er_{0.2}Y_{0.2}Gd_{0.2})PO₄ were synthesized by a chemical co-precipitation method using Lu₂O₃ (99.99%, Alfa Aesar), Yb₂O₃ (99.99%, Alfa Aesar), Fr₂O₃ (99.99%, Alfa Aesar), Y₂O₃ (99.99%, Alfa Aesar), Gd₂O₃ (99.99%, Alfa Aesar), 70 wt.% HNO₃ and 85 wt.% H₃PO₄ as the starting materials. The chemical reactions are presented in equations 3 and 4.

$$RE_2O_3(s) + 6 HNO_3(1) \rightarrow 2 RE(NO_3)_3(aq) + 3 H_2O(1)$$
 (3)

$$RE(NO_3)_3 (aq) + H_3PO_4 (1) \rightarrow REPO_4 (aq) + 3HNO_3 (1)$$
 (4)

RE₂O₃ was added to 0.2 mol/L HNO₃ in a 1:6 mole ratio with excess HNO₃ added so that RE₂O₃ would be the limiting reactant and the solution was then heated at 90 °C for 3 hours to obtain RE(NO₃)₃ solutions. Once the RE(NO₃)₃ solutions were obtained, H₃PO₄ was then added to the solution in a 1:1 mole ratio with RE(NO₃)₃ plus excess H₃PO₄ to ensure the complete conversion of the RE(NO₃)₃ in the solution to form the REPO₄ precipitate. The solution was

continuously stirred with a magnetic stir rod during the entire process to ensure that the solution was homogeneous. The REPO₄ precipitate was filtered from the solution using an 11 µm pore size filter paper and rinsed several times using deionized water to remove any excess acid. The precipitates were then dried at 90 °C for 12 hours, crushed into fine powders using a mortar and pestle, and then calcined at 1000 °C for 12 hours. LuPO₄ and YPO₄ powders were also prepared using the previously mentioned process.

2.2 $(Lu_{0.2}Yb_{0.2}Er_{0.2}Y_{0.2}Gd_{0.2})PO_4$ Pellet Sintering

The REPO₄ pellets were fabricated by loading approximately 0.8 g of finely ground calcined powders into 10 mm diameter cylindrical graphite dies and sintering them into dense pellets using an SPS (Model 10–3 SPS system, Thermal Tech. LLC, Santa Rosa, CA), under a steady flow of argon gas (1 L min⁻¹) to purge the chamber to avoid oxidation and degradation of graphite dies. All REPO₄ pellets were sintered at 1500 °C and 50 MPa for 5 minutes with a heating and cooling rate of 200 °C min⁻¹. Next, the pellets were ground with SiC abrasive papers and then polished using a 1 μm diamond paste to achieve a mirror finish with water acting as the polishing agent.

2.3 Structure, Phase, and Thermal Properties Characterization of (Lu_{0.2}Yb_{0.2}Er_{0.2}Y_{0.2}Gd_{0.2})PO₄

The phase composition of the calcined powder was confirmed via X-ray diffraction (XRD) using a Panalytical X'Pert Pro system (Westborough, MA, USA) with a copper target (Kα = 0.15406 nm) and a step size of 0.013°. Phase stability was determined by thermogravimetric analysis (TGA) using the TGA-Q50 system (TA instruments, New Castle, DE). Approximately 30 mg of (Lu_{0.2}Yb_{0.2}Er_{0.2}Y_{0.2}Gd_{0.2})PO₄ powders were weighed and placed in an alumina crucible and then heated in an argon atmosphere at a rate of 10 K min⁻¹ from room temperature to 1250 K. The CTE of the (Lu_{0.2}Yb_{0.2}Er_{0.2}Y_{0.2}Gd_{0.2})PO₄, LuPO₄ and YPO₄ pellets were determined by thermal dilatometry (DIL 402 Expedis Supreme, NETZCH, Germany) where the pellets were heated from room temperature to 1550 K at a heating rate of 10 K min⁻¹. The density of the pellets was measured via the Archimedes technique using an Adam analytical scale (Danbury, NY, USA) with deionized water as the immersing medium. The thermal

diffusivity of the REPO₄ pellets were measured with a laser flash apparatus (LFA) (LFA-457, NETZCH, Bavaria, Germany). Before LFA measurement, both sides of a pellet were polished to a mirror finish and uniformly coated with spray graphite paste to improve laser energy absorption and emissivity. The samples were heated at a rate of 5 °C min⁻¹, and their thermal diffusivities were evaluated using the Cape-Lehmann method based on a non-linear regression model from 345 to 1250 K. The specific heat capacity (c_p) of (Lu_{0.2}Yb_{0.2}Er_{0.2}Y_{0.2}Gd_{0.2})PO₄ was estimated by applying the Neumann-Kopp rule of mixtures using the constituent single component rare earth phosphates according to the chemical compositions [27, 28, 29, 30, 31]. The thermal conductivity k (W m⁻¹ K⁻¹) was calculated using Eq. (5), where ρ is the density of the sample pellet and α is thermal diffusivity (mm²·s⁻¹).

$$k = \alpha \rho c_P \tag{5}$$

2.4 CMAS Synthesis and Corrosion Testing

The CMAS composition used in this study is (mol%) 40CaO-5MgO-5AlO_{1.5}-50SiO₂, with CaO (99.99%, Sigma-Aldrich), MgO (99.99%, Sigma-Aldrich), Al₂O₃ (99.99%, Sigma-Aldrich), and SiO₂ (99.9%, Alfa Aesar) being used as the starting materials. This CMAS composition is a simplified version of the CMAS used in previous studies [7, 32], which is based on the composition of sand. The precursor powders were combined in a Pt crucible according to their stoichiometric ratios and heated to 1500 °C for 8 hours at a heating rate of 10 °C min⁻¹ then quenched in water to produce the CMAS glass. The CMAS glass was ground to attain uniform granularity, and it was then placed at the center of the polished top surface of the REPO₄ pellet at ~40 mg cm⁻² loading and heated in a box furnace at a rate of 10 °C min⁻¹ in air and cooled at a rate of 10 °C min⁻¹. The phase compositions of the CMAS corroded samples were confirmed by XRD. The samples after testing were then mounted in epoxy and cut in half to reveal the sample cross sections, after which they were polished to a mirror finish before SEM analysis. The Zeiss SUPRA 55 SEM equipped with an energy dispersive X-ray spectroscopy (EDS) detector was used to analyze the microstructure at the sample cross-section and perform EDS mapping and point identification.

3. Results

3.1 Thermal Properties and Phase Stability of (Lu_{0.2}Yb_{0.2}Er_{0.2}Y_{0.2}Gd_{0.2})PO₄

Fig. 1. shows the x-ray diffraction pattern of the synthesized (Lu_{0.2}Yb_{0.2}Er_{0.2}Y_{0.2}Gd_{0.2})PO₄ powders and sintered pellet. The indexed reflection indicates that the synthesized powders are single phase and of the xenotime structure. Figure 1 also shows XRD patterns of single component REPO₄ (RE = Lu, Yb, Er, Y, and Gd) obtained from ICDD/JCPDS cards, all of which exhibit the xenotime structure except for GdPO₄ which has the monazite structure. The lattice parameters of $(Lu_{0.2}Yb_{0.2}Er_{0.2}Y_{0.2}Gd_{0.2})PO_4$ (a = 6.878 Å and c = 6.023 Å.) were calculated using MDI Jade 6.5 through XRD refinement. These lattice parameter values are within the ranges of values for ErPO₄ (a = 6.863 Å and c = 6.007 Å) and HoPO₄ (a =6.887 Å and c = 6.024 Å). Similarly, the average cation ionic radius of the rare earth elements used to synthesize (Lu_{0.2}Yb_{0.2}Er_{0.2}Y_{0.2}Gd_{0.2})PO₄ (114.8 pm) is also between the ionic radii of $\mathrm{Er^{3+}}$ (114.40 pm) and $\mathrm{Ho^{3+}}$ (115.5 pm). This suggests that the average cation ionic radius is well correlated with the lattice parameter, and the lattice structure can accommodate the larger-sized cations such as Gd³⁺ which are too large to form the xenotime phase [33]. This has been demonstrated by Yang et al. (2021) through the study of equimolar multicomponent titanate pyrochlores, which showed a linear correlation between lattice parameter and average cation ionic radius [34]. Supplemental Figs. S1-2. show the x-ray diffraction patterns of the sintered LuPO₄ and YPO₄ pellets respectively, which confirms that both samples are single phase and of the xenotime structure.

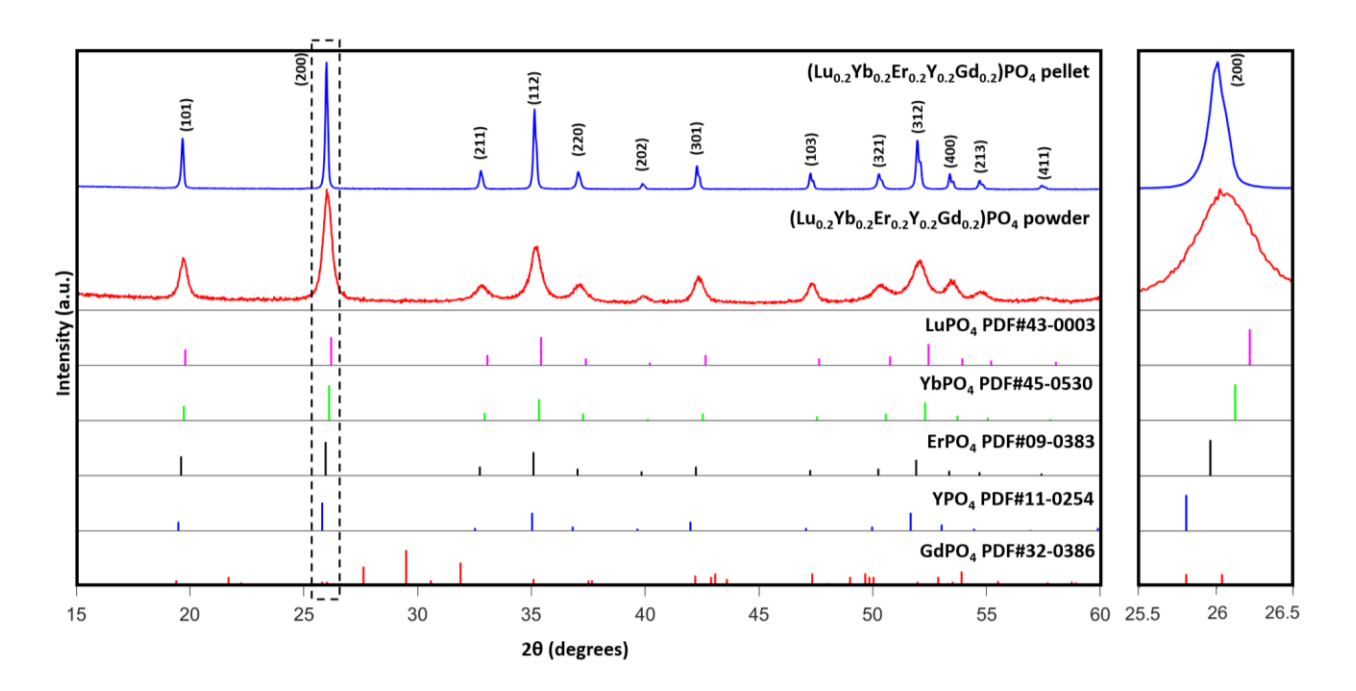


Fig. 1. XRD patterns of the $(Lu_{0.2}Yb_{0.2}Er_{0.2}Y_{0.2}Gd_{0.2})PO_4$ powders and the sintered pellet. The diffraction patterns of single component phosphates from ICDD/JCPD database are also included for comparison. The 25.5-26.5 2θ region highlighted by the dashed lines is shown in detail on the right side of the figure. It indicates the position of the $(Lu_{0.2}Yb_{0.2}Er_{0.2}Y_{0.2}Gd_{0.2})PO_4$ powder and sintered pellet's (200) reflection relative to that of the single component phosphates.

Fig. 2(A) shows the TGA curve of (Lu_{0.2}Yb_{0.2}Er_{0.2}Y_{0.2}Gd_{0.2})PO₄ powder during the heating from room temperature to 1250 K. The mass loss is less than 0.4% up to 1250 K, indicating no phase decomposition. Fig. 2(B) displays the temperature dependence of CTE for the (Lu_{0.2}Yb_{0.2}Er_{0.2}Y_{0.2}Gd_{0.2})PO₄, LuPO₄, and YPO₄ pellets from 400 to 1550 K. The CTE value of (Lu_{0.2}Yb_{0.2}Er_{0.2}Y_{0.2}Gd_{0.2})PO₄ varies from 3.9–6.8×10⁻⁶ K⁻¹ over this temperature range compared to 3.6-6.5×10⁻⁶ K⁻¹ and 3.3-6.5×10⁻⁶ K⁻¹ for LuPO₄ and YPO₄, respectively. Fig. 2(C) shows the measured thermal diffusivities of (Lu_{0.2}Yb_{0.2}Er_{0.2}Y_{0.2}Gd_{0.2})PO₄, LuPO₄, and YPO₄ from 350 K to 1250 K. These thermal diffusivities are used to calculate the thermal conductivities indicated in Fig. 2(D). At 1250 K, the thermal conductivity values of (Lu_{0.2}Yb_{0.2}Er_{0.2}Y_{0.2}Gd_{0.2})PO₄, LuPO₄, and YPO₄ are 2.86, 4.09, and 4.00 W m⁻¹ K⁻¹ respectively.

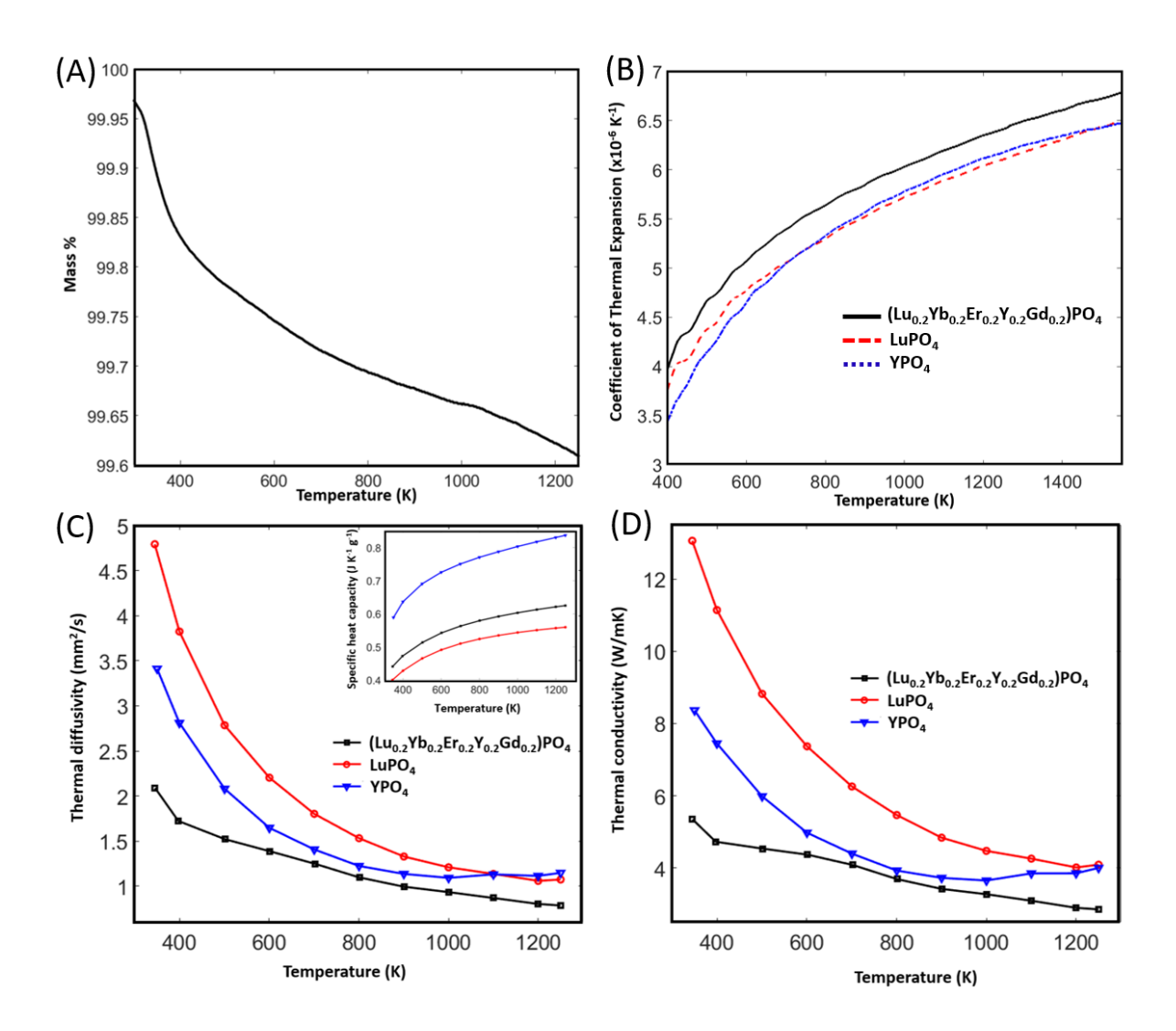


Fig. 2. (A) Thermogravimetric analysis curve of (Lu_{0.2}Yb_{0.2}Er_{0.2}Y_{0.2}Gd_{0.2})PO₄ powder from room temperature to 1250 K with a temperature increasing rate of 10 K/min in an argon atmosphere. (B) CTE of (Lu_{0.2}Yb_{0.2}Er_{0.2}Y_{0.2}Gd_{0.2})PO₄, LuPO₄, and YPO₄ in the temperature range of 400-1550 K. (C) Thermal diffusivity of (Lu_{0.2}Yb_{0.2}Er_{0.2}Y_{0.2}Gd_{0.2})PO₄, LuPO₄, and YPO₄ and YPO₄ and (D) thermal conductivity of (Lu_{0.2}Yb_{0.2}Er_{0.2}Y_{0.2}Gd_{0.2})PO₄, LuPO₄, and YPO₄ over the temperature range of 350-1250 K.

Fig. 3. shows the XRD patterns of the surface of (Lu_{0.2}Yb_{0.2}Er_{0.2}Y_{0.2}Gd_{0.2})PO₄ pellet before and after CMAS exposure for 5, 25, and 45 hours at 1300 °C. The diffraction peaks of the original pellet material were indexed as well as the reaction products Ca₈MgRE(PO₄)₇, Ca₂RE₈(SiO₄)₆O₂, and Ca₂MgSi₂O₇, which showed more intense peaks at longer durations. Ca₈MgEr(PO₄)₇ and Ca₂Er₈(SiO₄)₆O₂ were used as the reference peaks to index the

Ca₈MgRE(PO₄)₇ and Ca₂RE₈(SiO₄)₆O₂ phases. There is also the likely formation of oxy-apatite phases with the general formula of Ca_{2+x}RE_{8-x}(PO₄)_x(SiO₄)_{6-x}O₂, which are in the same P6₃/m (No. 176) space group as Ca₂RE₈(SiO₄)₆O₂ and are difficult to distinguish from each other through XRD analysis [35]. The RE₂Si₂O₇ that is often formed from the reaction between REPO₄ and CMAS was not observed at any duration.

3.2 Effects of Duration on the (Lu_{0.2}Yb_{0.2}Er_{0.2}Y_{0.2}Gd_{0.2})PO₄-CMAS Reaction

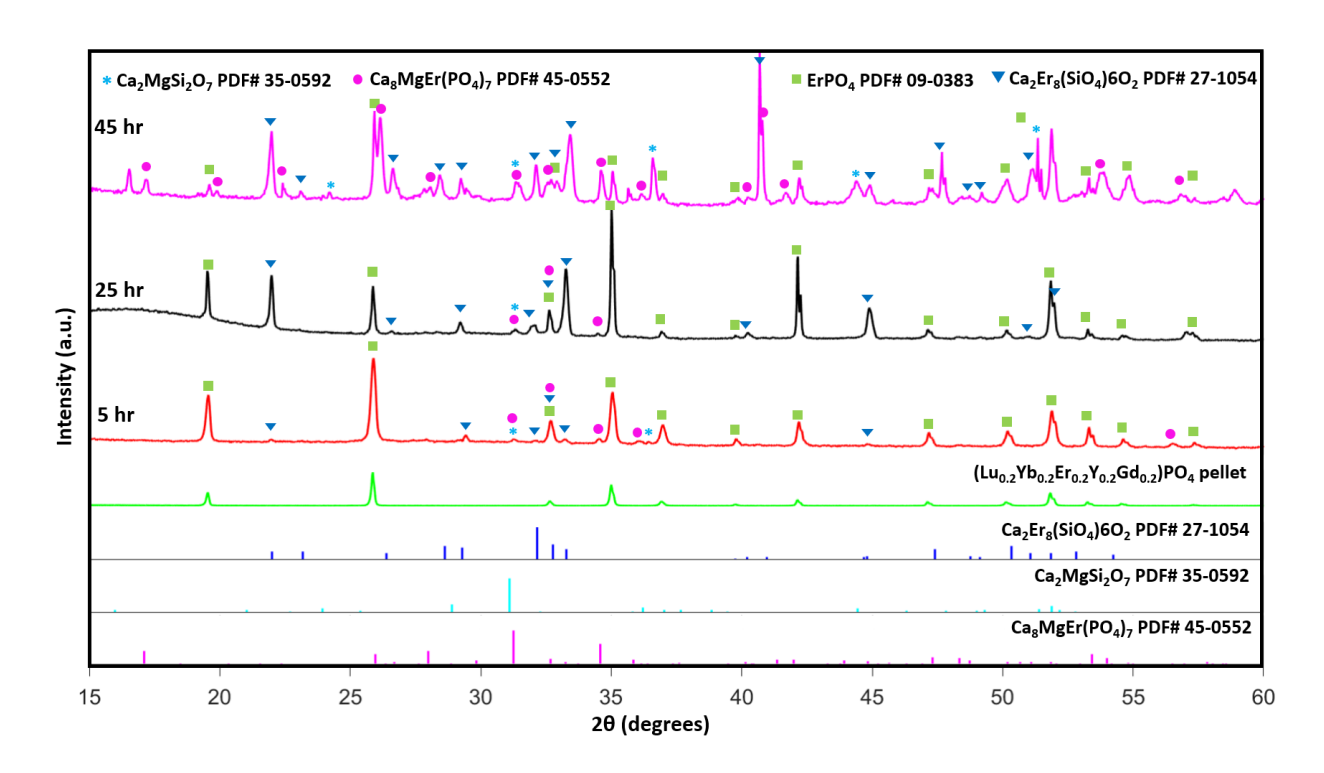


Fig. 3. XRD patterns of $(Lu_{0.2}Yb_{0.2}Er_{0.2}Y_{0.2}Gd_{0.2})PO_4$ after reaction with molten CMAS at 1300 °C for 5, 25, and 45 hours.

Fig. 4 displays the backscattered SEM images of the (Lu_{0.2}Yb_{0.2}Er_{0.2}Y_{0.2}Gd_{0.2})PO₄ pellet cross-section after 5 hours of CMAS corrosion at 1300 °C. The SEM images show the residual CMAS layer, and the bulk pellet separated by a uniform and dense reaction layer that is approximately $15.4 \pm 1.9 \, \mu m$ thick, with little to no CMAS penetrating past the reaction layer. Region 2 indicates the lighter contrast dendrite-like precipitates that are formed within the residual CMAS highlighted by region 1. Regions 3 and 4 indicate the lighter contrast top section and darker contrast bottom section of the reaction layer. The difference in Z contrast indicates a

difference in chemical composition within the reaction layer, while the unreacted bulk pellet is indicated by region 5. The EDS maps of the region in Fig. 4(A) are also displayed, where Ca and Si are predominantly relegated to the residual CMAS and the reaction layer. However, Ca appears to be more enriched within the reaction layer than within the residual CMAS. While still concentrated within the bulk pellet, the rare earth elements appear to be enriched in the top region of the reaction layer and in the precipitates found in the residual CMAS. Phosphorus is enriched within the bulk pellet but even more so within the reaction layer. Table 1 lists the chemical composition in atom % of the regions labeled in Figs. 4(A)-(B) plus an additional column labeled (REEs) which is the total atom % of all the rare earth elements. Region 2 mainly consists of Si, Ca, REEs, and P, and in conjunction with the XRD patterns, it is assumed to be Ca₃RE₇(PO₄)(SiO₄)₅O₂, though the Ca and REEs atom % are significantly different from what is expected for that phase. This is possibly due to the EDS detector collecting some of the signals from the surrounding CMAS. This is likely the case in region 3 which has a slightly higher quantity of Si and a smaller quantity of REEs but is assumed to be the same Ca₃RE₇(PO₄)(SiO₄)₅O₂ phase. While region 4 is composed of mostly Ca and P with small amount of REEs and Mg indicating a possible Ca₈MgRE(PO₄)₇ phase.

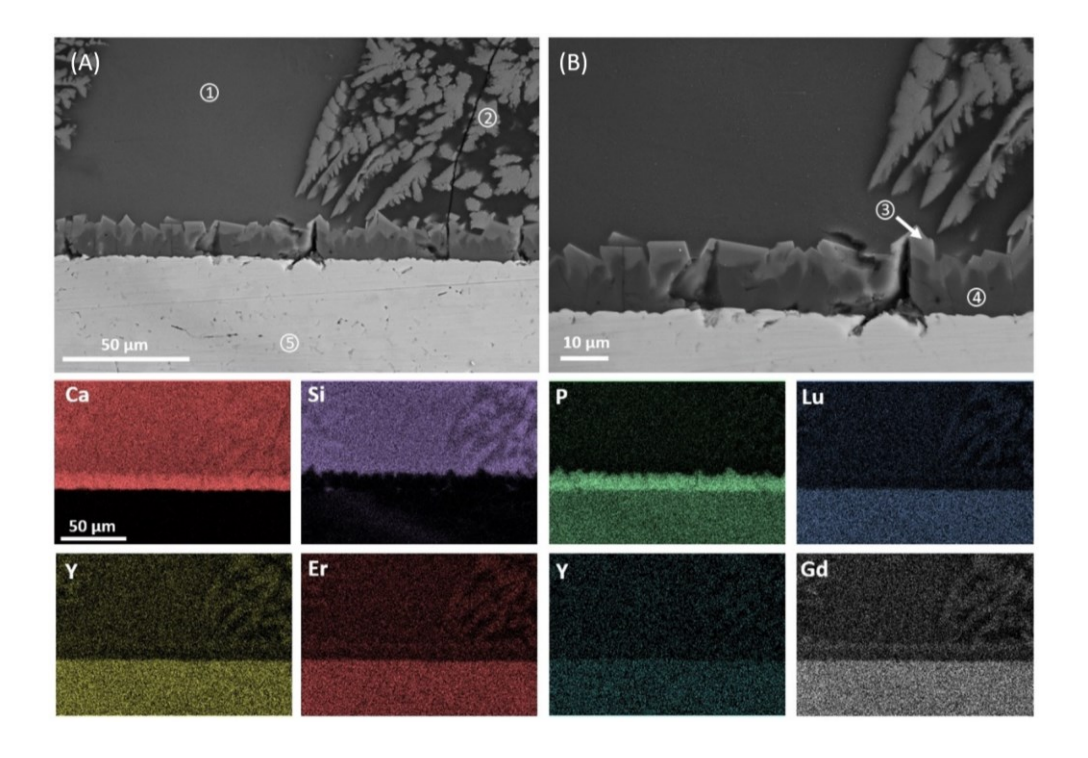


Fig. 4. SEM backscattered electron images of the cross-section and the corresponding EDS elemental maps of (Lu_{0.2}Yb_{0.2}Er_{0.2}Y_{0.2}Gd_{0.2})PO₄ interaction with molten CMAS at 1300 °C for 5 hours: (A) low and (B) high magnification images of the reaction layer.

Table 1. Chemical compositions (at. %) from the marked regions shown in Fig. 4.

Region	Mg	Al	Si	P	Ca	Y	Gd	Er	Yb	Lu	0	REEs
1	2.1	1.9	17.3	3.8	9.0	0.4	0.6	0.7	0.7	0.8	62.8	3.2
2	1.2	0.6	14.1	3.7	8.2	1.8	1.9	2.0	2.0	2.1	62.4	9.8
3	1.4	0.8	17.1	1.7	9.7	1.1	1.5	1.5	1.6	1.7	61.9	7.4
4	2.1	-	6.7	11.9	13.3	0.5	0.8	0.6	0.5	0.5	63.0	3.0
5	-	-	-	17.1	-	2.2	3.1	3.3	3.1	3.5	67.7	15.2

Fig. 5 presents the backscattered electron images of the cross-sectional view of the $(Lu_{0.2}Yb_{0.2}Er_{0.2}Y_{0.2}Gd_{0.2})PO_4$ pellet after the CMAS corrosion at $1300\,^{\circ}\text{C}$ for 25 hours. The dense reaction layer between the residual CMAS and the bulk pellet is still observed, however, the thickness increases to $29.1\pm4.5\,\mu\text{m}$ and there is still minimal CMAS penetration past the reaction layer. Unlike the cross-sectional view from the 5-hour corrosion pellet, no major dendrite precipitates were seen in the residual CMAS, but this could be due to the cross-section cut not passing through any large precipitates, as the $Ca_2RE_8(SiO_4)_6O_2/$

Ca_{2+x}RE_{8-x}(PO₄)_x(SiO₄)_{6-x}O₂ phase is confirmed from the XRD analysis. There is also some delamination of the reaction layer from the bulk pellet, but since this was only observed in this sample it is most likely due to the mechanical polishing before SEM characterization. EDS maps of the region in Fig. 5(A) similarly show that Ca and Si are regulated to the residual CMAS and the reaction layer, where Ca is more enriched. The rare earth elements are still concentrated within the bulk pellet with a slight enrichment at the top region of the reaction layer and within the residual CMAS, with phosphorus being enriched within the bulk pellet but more so within the reaction layer. The chemical compositions of regions 1 to 4 are listed in Table 2. Similar to the 5-hour corrosion experiment, the top section of the reaction layer (region 2) consists mainly of Si, REEs, Ca, and P, and is assumed to be Ca₃RE₇(PO₄)(SiO₄)₅O₂. While region 3 mainly

consists of Ca and P, and in conjunction with the XRD measurement, is assumed to be Ca₈MgRE(PO₄)₇.

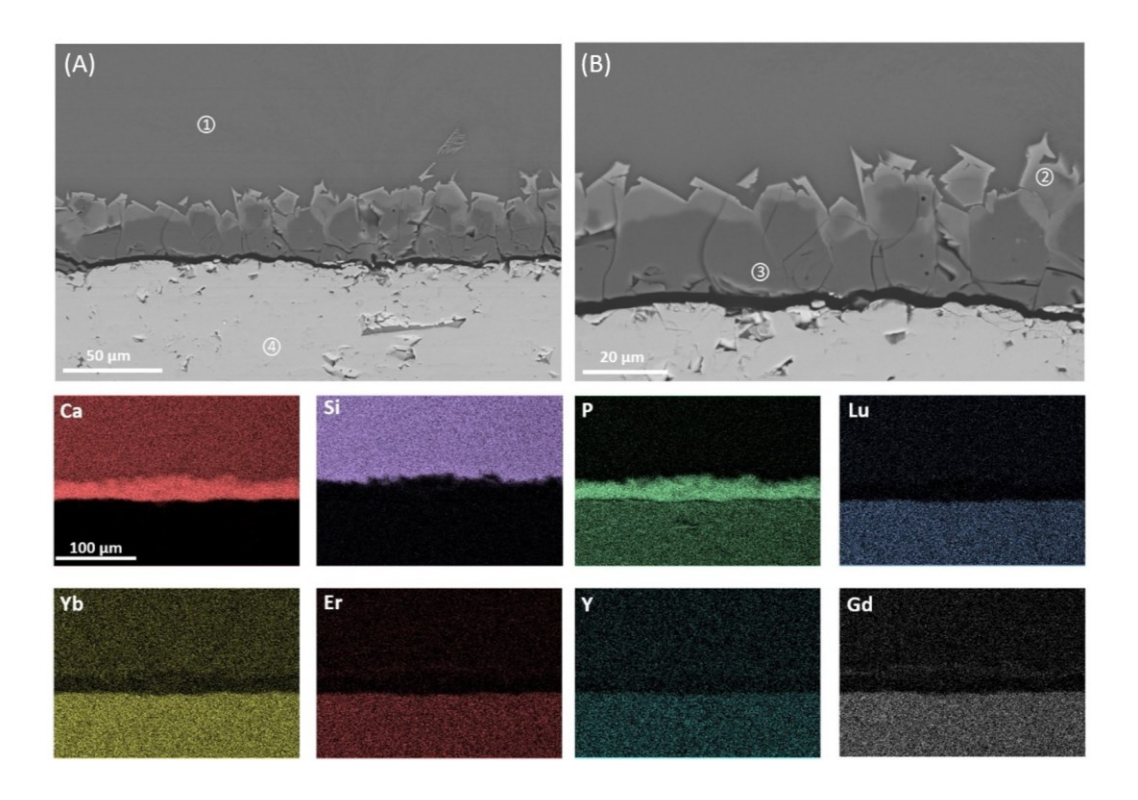


Fig. 5. SEM backscattered electron images of the cross-section and the corresponding EDS elemental maps of (Lu_{0.2}Yb_{0.2}Er_{0.2}Y_{0.2}Gd_{0.2})PO₄ interaction with molten CMAS at 1300 °C for 25 hours: (A) low and (B) high magnification images of the reaction layer.

Table 2. Chemical compositions (at. %) from the marked regions shown in Fig. 5.

Region	Mg	Al	Si	P	Ca	Y	Gd	Er	Yb	Lu	О	REEs
1	1.8	1.9	18.0	2.7	9.8	0.6	0.6	0.7	0.7	0.8	62.3	3.5
2	2.5	-	16.2	3.8	6.7	1.2	1.6	1.8	1.8	1.9	62.4	8.4
3	2.2	-	1.4	14.6	16.4	0.5	0.8	0.7	0.6	0.6	62.6	3.1
4	-	-	-	17.4	0.1	2.5	3.0	3.4	3.2	3.6	66.9	15.6

Fig. 6 shows the backscattered electron images and corresponding EDS maps of the (Lu_{0.2}Yb_{0.2}Er_{0.2}Y_{0.2}Gd_{0.2})PO₄ pellet in the cross-sectional view post-CMAS corrosion at 1300 °C for 45 hours. The CMAS-pellet interaction region still consists of a dense reaction layer between the residual CMAS and the bulk pellet which is now approximately $39.7 \pm 8.4 \,\mu m$ thick and comprises of three different regions based on the contrast variation. Similar to the 5 and 25-hour experiments, the reaction layer appears to halt the CMAS penetration into the bulk pellet, as there appears to be little to no CMAS in the pores below the reaction layer. There is also a noticeable increase in the quantity and size of precipitates within the residual CMAS as compared to the 5 and 25-hour experiments. Based on the EDS maps of the region in Fig. 6(A), the top section of the reaction layer appears to be enriched in Si and REEs but slightly depleted in Ca and P relative to the bottom section of the reaction layer, which is enriched in Ca and P, and depleted in Si and REEs. The dendrite-like precipitates on the other hand seem to be enriched in Ca, REEs, and Si. Table 3 lists the chemical compositions of the different regions highlighted in Fig. 6(A)-(B) Similar to the 5-hour experiment, the dendrite-like precipitates at region 2 mainly consist of Si, Ca, and REEs. Based on the XRD result, this is also presumed to be Ca₂RE₈(SiO₄)₆O₂ with some additional signals from the surrounding CMAS. This is likely also the case for region 3 which shows a similar chemical composition. Region 4 is mainly composed of P, Ca, REEs, and Si, and is inferred to be a variation of the Ca₈MgRE(PO₄)₇ phase; where there is a partial substitution of the PO₄ tetrahedra by the SiO₄ tetrahedra forming an offstoichiometry phase, likely Ca_{6.5}MgRE_{2.5}(SiO₄)_{1.5}(PO₄)_{5.5} based on the ratio of P to Si. Region 5 is ascertained to be Ca₈MgRE(PO₄)₇ based on the element ratio and the XRD measurement. The chemical composition at region 6 is indicative of the bulk pellet and indicates no significant CMAS penetration past the reaction layer after 45 hours.

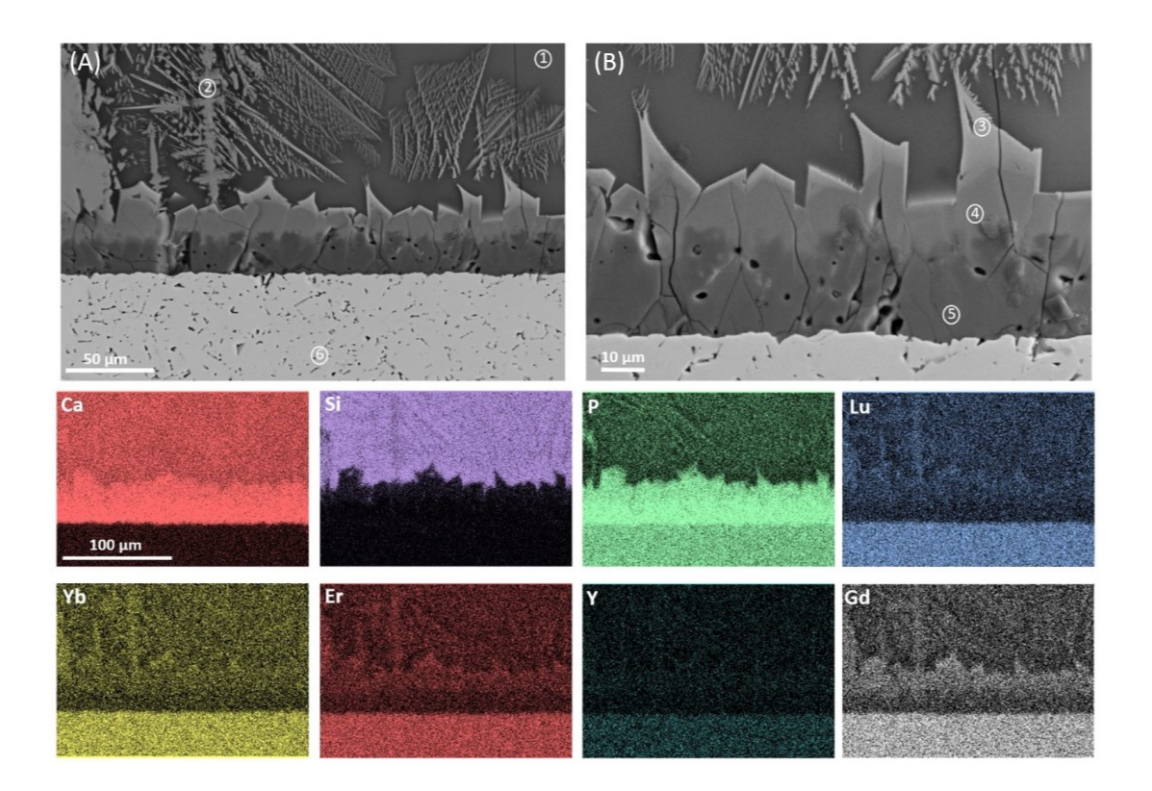


Fig. 6. SEM backscattered electron images of the cross-section and the corresponding EDS elemental maps of (Lu_{0.2}Yb_{0.2}Er_{0.2}Y_{0.2}Gd_{0.2})PO₄ interaction with molten CMAS at 1300 °C for 45 hours: (A) low and (B) high magnification images of the reaction layer.

Table 3. Chemical compositions (at. %) from the marked regions shown in Fig. 6.

Region	Mg	Al	Si	P	Ca	Y	Gd	Er	Yb	Lu	0	REEs
1	2.5	2.4	18.0	2.4	9.0	0.6	0.6	0.7	0.7	0.8	62.3	3.3
2	0.6	0.6	16.8	2.5	10.5	1.2	1.2	1.4	1.4	1.5	62.3	6.7
3	3.2	-	15.8	1.4	9.4	1.5	1.4	1.6	1.7	1.8	62.2	8.0
4	1.9	-	4.1	11.9	14.8	1.0	1.4	1.1	0.9	0.9	62.2	5.2
5	1.5	-	0.2	16.1	17.2	0.5	0.5	0.5	0.4	0.4	62.7	2.3
6	-	-	-	16.5	-	3.0	3.3	3.5	3.4	3.7	66.6	16.8

The increase in the duration of the $(Lu_{0.2}Yb_{0.2}Er_{0.2}Y_{0.2}Gd_{0.2})PO_4$ -CMAS reaction at 1300 °C leads to a clear increase in the reaction layer thickness. The growth rate of the reaction layer

thickness decreases with longer reaction durations, as evidenced by the 23% reduction in growth from 25 to 45 hours compared to the growth from 5 to 25 hours. The average thickness of these reaction layers was plotted against the square root of time in Fig. 7(A). A linear relation is identified between the reaction layer thickness and the square root of time with a rate constant calculated as $5.4 \pm 0.3~\mu m$ h^{-0.5}. The linear relation suggests a diffusion-controlled mechanism for the formation of the interfacial layer upon the reaction of the CMAS with the phosphate matrix.

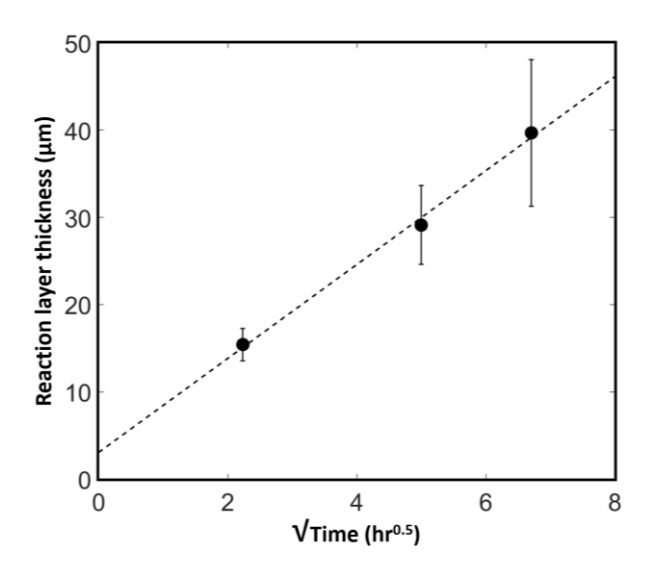


Fig. 7. Average reaction layer thickness plotted against the square root of time for the $(Lu_{0.2}Yb_{0.2}Er_{0.2}Y_{0.2}Gd_{0.2})PO_4$ -CMAS interactions at 1300 °C.

3.3 Effects of Temperature on the $(Lu_{0.2}Yb_{0.2}Er_{0.2}Y_{0.2}Gd_{0.2})PO_4$ -CMAS Reaction

Fig. 8 shows the XRD patterns at the (Lu_{0.2}Yb_{0.2}Er_{0.2}Y_{0.2}Gd_{0.2})PO₄ pellet surface layer before and after CMAS reaction for 5 hours at 1400 °C and 1500 °C. At 1400 °C the diffraction peaks indicate the formation of Ca₈MgRE(PO₄)₇ and cristobalite (SiO₂) phases, while no Ca₂RE₈(SiO₄)₆O₂ and Ca₂MgSi₂O₇ phases are present. This indicates a change in the (Lu_{0.2}Yb_{0.2}Er_{0.2}Y_{0.2}Gd_{0.2})PO₄-CMAS reaction mechanism with increased temperature, in which the phosphate-based apatite is more energetically favorable than the silicate-based apatite with the dissolution of more phosphorus in CMAS at higher temperatures. The diffraction patterns

obtained from the pellet surface after the (Lu_{0.2}Yb_{0.2}Er_{0.2}Y_{0.2}Gd_{0.2})PO₄-CMAS reaction after 5 hours at 1500 °C also show the formation of the cristobalite phase, however, no other phases were detected by the XRD measurements which indicates a difference in the reaction mechanisms at 1400 and 1500 °C.

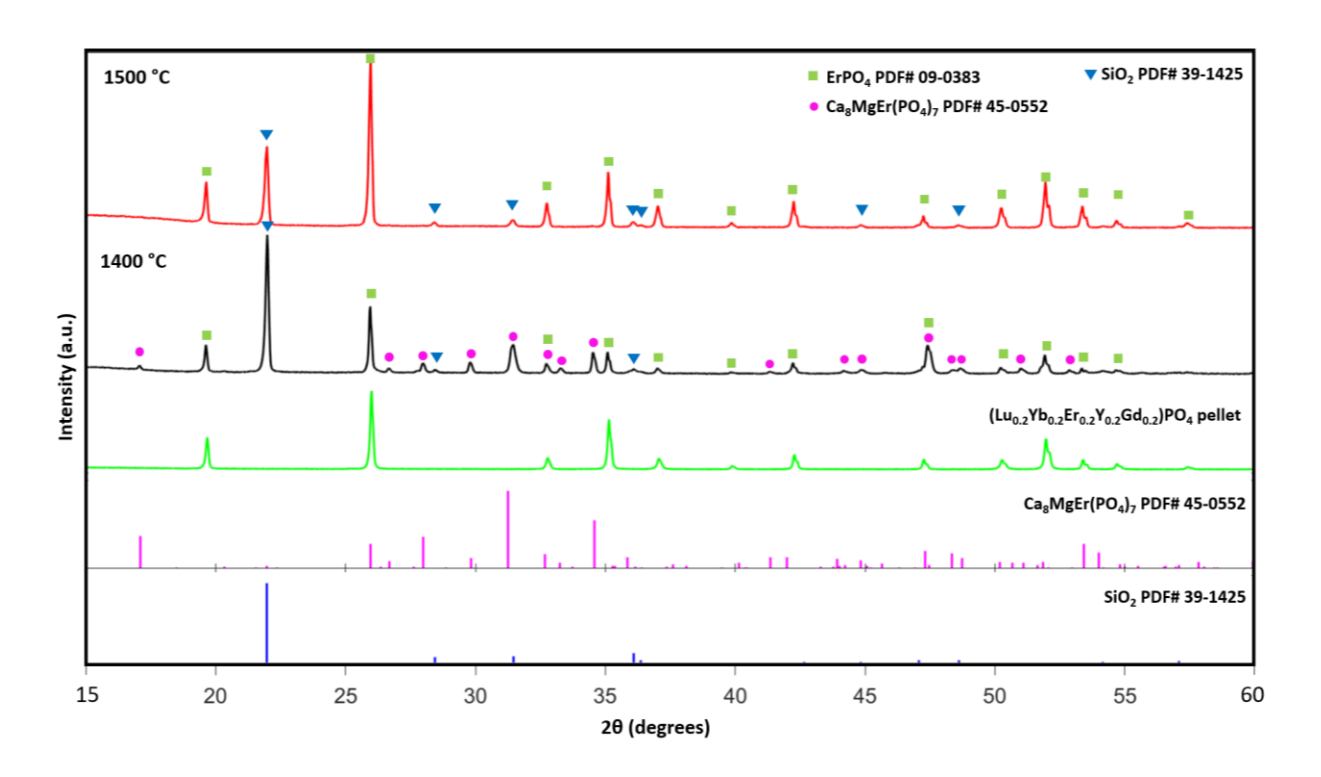


Fig. 8. XRD patterns of (Lu_{0.2}Yb_{0.2}Er_{0.2}Y_{0.2}Gd_{0.2})PO₄ after reaction with molten CMAS at 1400 °C and 1500 °C for 5 hours.

The SEM cross-sectional images of the (Lu_{0.2}Yb_{0.2}Er_{0.2}Y_{0.2}Gd_{0.2})PO₄-CMAS interaction at 1400 °C for 5 hours are displayed in Fig. 9. The reaction layer formed during this interaction is much larger compared to the reaction at 1300 °C for the same duration, however, it is less uniform varying between 20-95 µm with the thinner region near the center of the pellet. There are also sparsely located dark contrast precipitates up to 45 µm in size in the reaction layer, these precipitates were confirmed to be cristobalite grains. The reaction layer is also less dense which leads to CMAS penetration through the reaction layer and into the pellet below, as seen in Fig. 9(B). The darker contrast of the CMAS is evident between the grains and inside the pores of the bulk pellet. There are also visible cracks and voids within the bulk pellet, which are not observed

in the reaction at 1300 °C, possibly due to the swelling caused by CMAS penetration along the grain boundaries. The EDS maps of the region in Fig. 9(B) show the enrichment of Ca within the reaction layer and in the voids below the reaction layer, which further confirms the penetration of the CMAS beyond the reaction layer. The rare earth elements are also present in the reaction layer; however, they are still concentrated within the bulk pellet. Si is heavily concentrated within the dark contrast precipitates and within the small quantity of residual CMAS left on top of the reaction layer as well as the CMAS that has penetrated into the bulk pellet. Table 4 presents the chemical compositions of the different regions highlighted in Fig. 9(B). The EDS analysis of the region 1 indicates that the residual CMAS is predominantly composed of Si and Ca; however, the Si content in this region is higher compared to the residual CMAS from the 1300 °C reaction for the same duration. Regions 2 and 3 are both assumed to be the Ca8MgRE(PO4)7 phase based on the XRD pattern and EDS compositions. These regions are mainly composed of Ca, P, and REEs, although the measured quantities of REEs are relatively high for this phase. The composition measured at region 4 confirms that the darker precipitates are cristobalite, while the composition measured at region 5 appears to be mainly the bulk pellet.

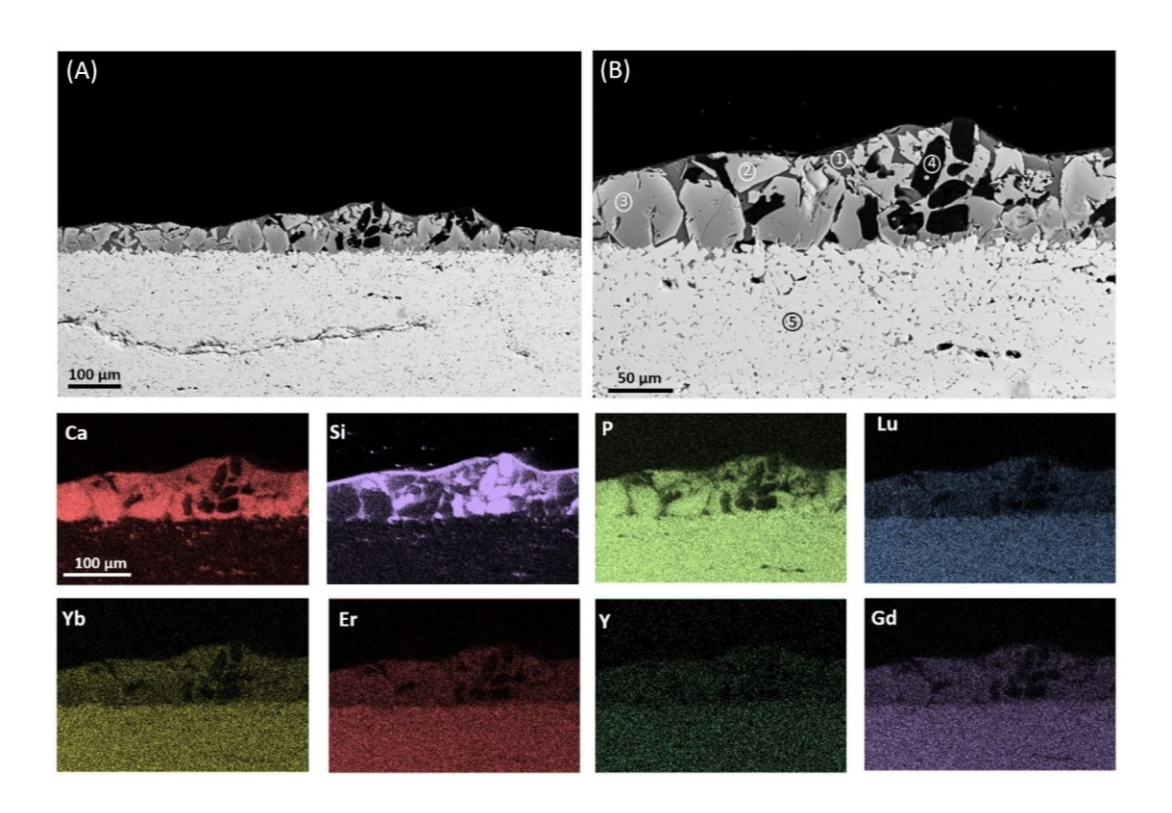


Fig 9. SEM backscattered electron images of the cross-section and the corresponding EDS elemental maps of (Lu_{0.2}Yb_{0.2}Er_{0.2}Y_{0.2}Gd_{0.2})PO₄ interaction with molten CMAS at 1400 °C for 5 hours: (A) low and (B) high magnification images of the reaction layer.

Table 4. Chemical compositions (at. %) from the marked regions shown in Fig. 9.

Region	Mg	Al	Si	P	Ca	Y	Gd	Er	Yb	Lu	0	REEs
1	2.1	1.3	21.5	1.7	8.4	0.5	0.4	0.6	0.5	0.7	62.3	2.7
2	1.7	-	4.1	11.5	14.1	1.2	1.5	1.3	1.2	1.2	62.3	6.3
3	1.6	-	4.3	11.8	14.1	1.0	1.5	1.2	1.1	1.1	62.4	5.8
4	-	-	33.3	-	-	-	-	-	-	-	66.7	-
5	-	-	-	16.5	-	3.0	3.0	3.6	3.5	3.8	66.6	16.9

Fig. 10(A) shows no reaction layer formed at the surface of the pellet after interacting with CMAS at 1500 °C for 5 hours, which was also confirmed by the lack of Ca₈MgRE(PO₄)₇ peaks from the XRD measurement. Instead, clear penetration of the CMAS into the bulk pellet via the grain boundaries is observed. Hence, there is an increase in the quantity and size of the voids formed within the bulk pellet as compared to the reaction at 1400 °C for 5 hours. A clear recession of the bulk pellet is observed, particularly at the center where the initial layer of CMAS melt would have been the largest. Fig. 10(B) is a high-magnification image from this location and confirms the clear penetration of CMAS into the pellet and the formation of darker contrast precipitates on the pellet surface, which are most likely cristobalite. The EDS maps of the region in Fig. 10(B) further confirm the penetration of CMAS into the bulk pellet as Ca is predominantly located between the pellet grains, where there appears to be some depletion of P and the REEs relative to the bulk pellet. However, the CMAS between the grains appears to contain little to no Si, as Si is only located in the precipitates on the pellet surface. The chemical composition at region 1 confirms that these precipitates are cristobalite as they contain no Ca, P, or REEs, while region 2 is the unreacted bulk pellet.

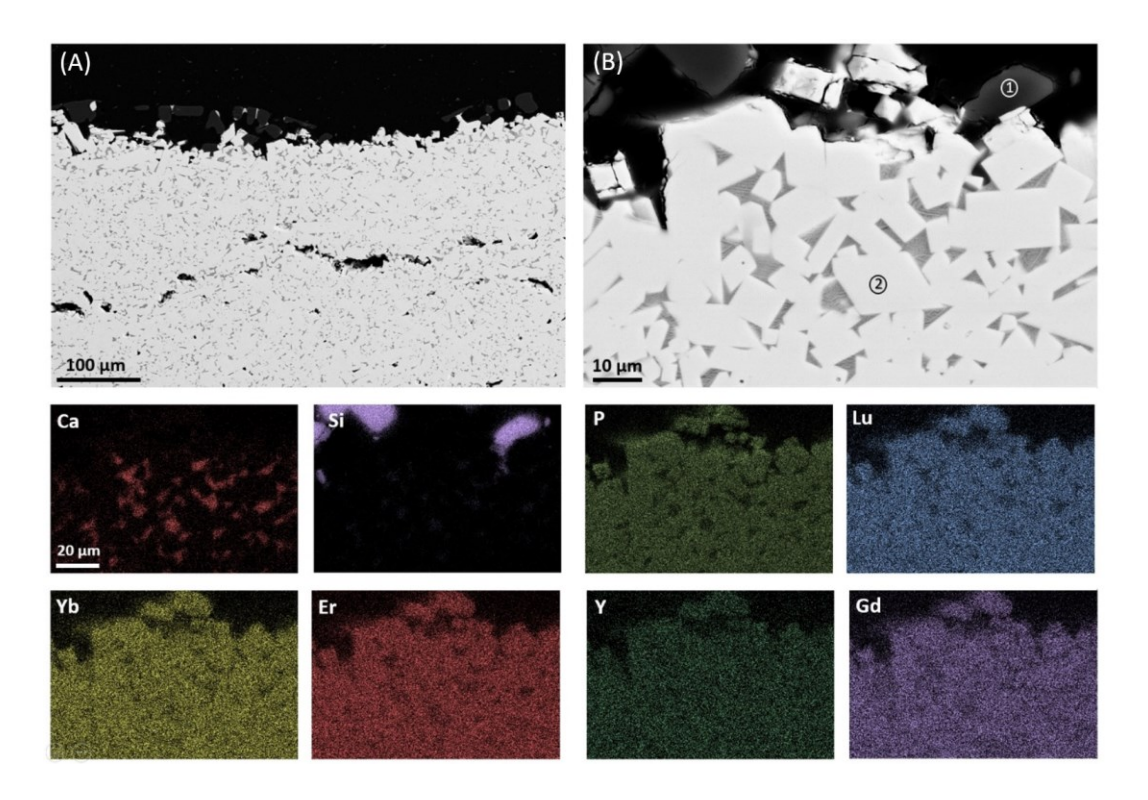


Fig 10. SEM backscattered electron images of the cross-section and the corresponding EDS elemental maps of (Lu_{0.2}Yb_{0.2}Er_{0.2}Y_{0.2}Gd_{0.2})PO₄ interaction with molten CMAS at 1500 °C for 5 hours: (A) low and (B) high magnification images of the pellet surface.

Table 5. Chemical compositions (at. %) from the marked regions shown in Fig. 10.

Region	Mg	Al	Si	P	Ca	Y	Gd	Er	Yb	Lu	О	REEs
1	-	-	29.9	-	-	-	-	-	-	-	70.1	-
2	-	-	-	17.5	0.5	2.5	2.6	3.1	3.0	3.3	67.6	14.4

4. Discussion

4.1 Thermal Properties of (Lu_{0.2}Yb_{0.2}Er_{0.2}Y_{0.2}Gd_{0.2})PO₄

The TGA curve of (Lu_{0.2}Yb_{0.2}Er_{0.2}Y_{0.2}Gd_{0.2})PO₄ powder showed less than 0.4 % mass loss from room temperature up to 1250 K, this gradual decrease in mass indicates no phase decomposition up to 1250 K. Higher temperature testing by the TGA analysis was not conducted due to the limit of the sample testing apparatus. However, the sample was sintered at 1500 °C

and the XRD diffraction patterns of the samples after CMAS testing also show the existence of the phosphate phase in addition to the reaction products, which will be discussed later. Therefore, multicomponent rare-earth phosphates show good thermal stability. The measured CTE values of (Lu_{0.2}Yb_{0.2}Er_{0.2}Y_{0.2}Gd_{0.2})PO₄ are close to those of LuPO₄ and YPO₄, over the range of 400 to 1550 K and match well with the CTE of SiC CMC (4.5–5.5×10⁻⁶ K⁻¹), making (Lu_{0.2}Yb_{0.2}Er_{0.2}Y_{0.2}Gd_{0.2})PO₄ a possible candidate for EBC application [18]. As shown in Fig. 2 (C), except for YPO₄ above 1000 K, the thermal conductivity for all three materials decreased steadily with temperature across the entire measurement range. This is a common feature of ceramics where heat transport is predominantly governed by phonon transport. However, the increase in thermal conductivity of YPO₄ at temperatures above 1000 K, indicates that electronic transport may be the dominant mechanism of heat transport at higher temperatures [17]. (Lu_{0.2}Yb_{0.2}Er_{0.2}Y_{0.2}Gd_{0.2})PO₄ showed a lower thermal conductivity than both LuPO₄ and YPO₄, and any of the single component xenotime phase rare earth phosphates (REPO₄, RE = Lu, Yb, Er, Y, and Sc) reported by Han et al. (2020) which ranged between 4.5-7.5 W m⁻¹ K⁻¹ at 1250 K [17]. This is a promising development as lowered thermal conductivity is a desirable feature for EBC materials as it reduces heat flow from the coating to the SiC substrate. The thermal conductivity of single phase multicomponent ceramic oxides has been the focus of several recent studies. Wright et al. (2020) investigated the effects of cation size disorder, cation mass disorder, and mixing entropy (Δs_{mix}) on the thermal conductivity of pyrochlores; while Yang et al. (2021) investigated the effects of these factors on the thermal conductivity of uranium doped titanate pyrochlores [23, 34]. Both studies found that thermal conductivity correlated most strongly with cation size disorder as having ions of different sizes at the same lattice position leads to lattice distortion and increases phonon scattering hence suppressing heat conduction. In this study, single phase (Lu_{0.2}Yb_{0.2}Er_{0.2}Y_{0.2}Gd_{0.2})PO₄ shows reduced thermal conductivity compared to all the xenotime phase rare earth phosphates (REPO₄, RE =Lu, Yb, Er, Y, and Sc), likely due to the increased phonon scattering from the distorted lattice.

4.2 Effects of Duration on the $(Lu_{0.2}Yb_{0.2}Er_{0.2}Y_{0.2}Gd_{0.2})PO_4$ -CMAS Interaction

Considering the results highlighted in the previous section, the reaction of (Lu_{0.2}Yb_{0.2}Er_{0.2}Y_{0.2}Gd_{0.2})PO₄ with CMAS at 1300 °C generally leads to the formation of a dense

and uniform multi-phase reaction layer between the residual CMAS and the bulk pellet as well as Ca₂RE₈(SiO₄)₆O₂ and possibly Ca₂MgSi₂O₇ precipitates within the residual CMAS. The multi-phase reaction layer is composed of stochiometric and off-stochiometric phases of Ca₈MgRE(PO₄)₇ and Ca₂RE₈(SiO₄)₆O₂, with the Ca₈MgRE(PO₄)₇ phases being most of the reaction layer and forming the lower region closest to the bulk pellet and the Ca₂RE₈(SiO₄)₆O₂ phases forming the regions closest to the residual CMAS.

$$7 REPO_4 + 8 CaO + MgO = Ca_8MgRE(PO_4)_7 + 3 RE_2O_3 + residual CMAS$$
 (6)

$$4 RE2O3 + 2 CaO + 6 SiO2 = Ca2RE8(SiO4)6O2$$
 (7)

Equation 6 represents the initial reaction which leads to the formation of the reaction layer through the dissolution of REEs and P into the residual CMAS region and the reprecipitation of Ca₈MgRE(PO₄)₇ at the interface between the bulk pellet and the residual CMAS. Gradually, the buildup of rare earth elements within the CMAS along with the abundant Ca and Si leads to the precipitation of Ca₂RE₈(SiO₄)₆O₂ at the top surface of the reaction layer and within the residual CMAS, according to equation 7. The precipitation of both phases is related to the dissolution of REPO4 into the CMAS melt. Since the concentration of the initially dissolved REEs and P is the highest at the interfacial region, the Ca₈MgRE(PO₄)₇ precipitate forms closest to the bulk pellet, and this phase likely precipitates at a faster rate than the Ca₂RE₈(SiO₄)₆O₂ phase. There is also the possibility of oxy-apatite phases being formed, where RE³⁺ and SiO₄⁴⁻ within the Ca₂RE₈(SiO₄)₆O₂ structure are partially substituted by Ca²⁺ and PO₄³⁻ or Ca²⁺ and PO₄³⁻ within the Ca₈MgRE(PO₄)₇ structure are partially substituted by RE³⁺ and SiO_4^{4-} . Thus, off-stoichiometric $Ca_{2+x}RE_{8-x}(PO_4)_x(SiO_4)_{6-x}O_2$ and $Ca_{8-x}MgRE_{1+x}(SiO_4)_x(PO_4)_{7-x}$ phases may form which are structurally similar to their more stoichiometric compositions [36]. The fast and energetically favorable precipitation of Ca₈MgRE(PO₄)₇ is also evident in the 1400 °C testing for 5 hours, as no Ca₂RE₈(SiO₄)₆O₂ is observed. A common reaction product of the REPO₄-CMAS interaction is the RE₂Si₂O₇ phase, which has been reported by Hu (2020) and Ridley (2022) who investigated the interaction of CMAS with LuPO₄ and YbPO₄, respectively [18, 19]. This phase was never observed by XRD or SEM-EDS for the (Lu_{0.2}Yb_{0.2}Er_{0.2}Y_{0.2}Gd_{0.2})PO₄ reaction with CMAS at any durations, which is likely due to the CMAS in this study having a higher Ca content (40 mol%) compared to the 33 mol% used in Hu and Ridley's studies. Increased Ca within the residual CMAS leads to the availability of Ca, REEs, and Si causing the precipitation of Ca₂RE₈(SiO₄)₆O₂ which consumes more REEs and Si than Ca. There is also no indication of the CaAl₂Si₂O₈ phase likely due to the reduced quantity of Al in the CMAS used in this study. Based on these results, it is likely that CMAS composition plays an integral role in determining which reaction products are formed when reacted with REPO₄, as CMAS varies in composition based on the sample sources and study-specific models. More systematic research is needed to identify the effects of each element within the CMAS on the reaction with REPO₄ [14].

Elemental analysis performed at the unreacted section of the (Lu_{0.2}Yb_{0.2}Er_{0.2}Y_{0.2}Gd_{0.2})PO₄ pellet shows a slight increase in Lu atom % and a slight decrease in Y atom % relative to the other rare earth elements in the pellet composition. This variation is likely due to a difference between the design composition and the nominal composition of the multicomponent rare earth phosphate. Based on the relative chemical composition of the rare earth elements in the unreacted pellet, there is little to no relative enrichment of the rare earth elements within the reaction products, except for a small increase in Gd and a decrease in Lu within the Ca₈MgRE(PO₄)₇ reaction layer at every experimental condition. As indicated by Fig. 7, there is a clear linear increase in the reaction layer thickness with the square root of time, where the reaction rate was 5.4 µm h^{-0.5}, which is comparable to the reaction rates of LuPO₄ (5.0 μm h^{-0.5}) and YbPO₄ (5.3 μm h^{-0.5}) obtained from the studies of Hu et al. (2020) and Ridley et al. (2022) respectively. However, a direct comparison cannot be made considering the difference in the CMAS composition and materials systems used in different studies [19, 20]. It is important to note that CaO is a limiting reactant in the formation of the Ca₈MgRE(PO₄)₇ reaction layer, and the increased Ca content of the CMAS used in this study likely increases the reaction layer thickness and the reaction rate. The difference in Ca and Al contents of the CMAS used in this study (40CaO-5MgO-5AlO_{1.5}-50SiO₂) likely causes a decrease in viscosity relative to the CMAS (33CaO-9MgO-13AlO_{1.5}-45SiO₂) used in Hu and Ridley's studies [18, 19, 37]. A decrease in viscosity leads to the CMAS having a higher penetration ability which would increase the reaction rate with the REPO₄. However, the degree to which this occurs has not yet been investigated.

4.3 Effects of Temperature on $(Lu_{0.2}Yb_{0.2}Er_{0.2}Y_{0.2}Gd_{0.2})PO_4$ -CMAS Interaction

The (Lu_{0.2}Yb_{0.2}Er_{0.2}Y_{0.2}Gd_{0.2})PO₄-CMAS interaction at 1400 °C for 5 hours shows significant differences compared to the interactions at 1300 °C. There is still the formation of the Ca₈MgRE(PO₄)₇ reaction layer; however, its thickness is less uniform compared to the reaction layer formed at 1300 °C for the same duration. The increase in reaction temperature increases the reaction between the (Lu_{0.2}Yb_{0.2}Er_{0.2}Y_{0.2}Gd_{0.2})PO₄ and the CMAS leading to the formation of a thicker reaction layer, particularly in the regions where the CMAS layer is thinner. Due to the increased temperature, there is also a significant decrease in the viscosity of the CMAS melt, leading to faster penetration of the CMAS into the bulk pellet. The rapid penetration of the CMAS into the pellet decreases the formation of the reaction layer as the REEs and P dissolve in the melt as it penetrates through the bulk pellet via the grain boundaries. The addition of REEs to the CMAS melt further decreases the viscosity of the melt, leading to faster penetration of the CMAS [37, 38].

Another notable difference from the low-temperature reactions is the formation of cristobalite precipitates at the surface of the bulk pellet, which has been observed in the reaction between rare earth disilicates and CMAS by Stokes et al. (2019) [39]. Stokes et al. (2021) investigated the melting and crystallization behavior of CMAS of various compositions and observed recrystallized cristobalite in CMAS with Si composition of 64 mol% and above, at temperatures of 1200-1400 °C after 1 hour [40]. The CMAS used in this study has an initial Si composition of approximately 50 mol%, which can recrystallize into cristobalite at 1400 °C. This could be a result of the rapid depletion of Ca as the Ca₈MgRE(PO₄)₇ reaction layer requires a substantial amount of Ca, which causes a relative increase in the quantity of Si leading to the recrystallization of cristobalite. Conversely, the quantity of REPO₄ needed to form the larger Ca₈MgRE(PO₄)₇ reaction layer should also produce a substantial amount of REEs. However, no REEs enriched phases are observed, and the remaining CMAS on top of the reaction layer is depleted in REEs. The dissolved REEs are likely contained in the CMAS melt that penetrated into the bulk pellet.

Once the reaction temperature increases to 1500 °C, CMAS melt viscosity is further decreased and the rate of penetration of the CMAS increases. This reduces the ability of the Ca₈MgRE(PO₄)₇ phase to precipitate at the surface of the pellet, and hence no reaction layer is

formed at the pellet surface. Although there is no reaction layer present at the pellet's top surface, there is still the formation of cristobalite grains and visible erosion of the bulk pellet indicating the dissolution of the rare earth phosphate in the CMAS. The lack of Si in the CMAS that has penetrated into the bulk pellet at 1500 °C as shown by the EDS mapping in Fig. 10 indicates that the recrystallization of the cristobalite likely occurs at a faster rate than the penetration of the CMAS into the pellet. According to the data presented by Stokes et al. (2021), 50 mol% SiO₂ should be too low to cause cristobalite recrystallization within the CMAS melt [40]. However, the rate of cristobalite recrystallization is likely affected by the comparative increase in temperature, heating duration, and interaction with the rare earth phosphate pellet. To our knowledge no studies have investigated the rare earth phosphate CMAS interaction at temperatures above 1300 °C at the time of submitting this manuscript, hence no direct comparisons can be made regarding the performance of the (Lu_{0.2}Yb_{0.2}Er_{0.2}Y_{0.2}Gd_{0.2})PO₄ at 1400 and 1500 °C. Overall, the (Lu_{0.2}Yb_{0.2}Er_{0.2}Y_{0.2}Gd_{0.2})PO₄ showed a comparable resistance to CMAS corrosion as LuPO₄ and YbPO₄ at 1300 °C with the added benefit of reduced thermal conductivity [18, 19].

5. Conclusions

In this study, we explored (Lu_{0.2}Yb_{0.2}Er_{0.2}Y_{0.2}Gd_{0.2})PO₄ as a potential EBC candidate material by investigating its thermal properties and its resistance to CMAS corrosion. The single phase xenotime structure (Lu_{0.2}Yb_{0.2}Er_{0.2}Y_{0.2}Gd_{0.2})PO₄ was synthesized via the chemical precipitation method and shows a comparable CTE to SiC CMC, and a lower thermal conductivity than any single component rare earth phosphates at 1250 K. (Lu_{0.2}Yb_{0.2}Er_{0.2}Y_{0.2}Gd_{0.2})PO₄-CMAS interactions were carried out at 1300 °C for 5, 25 and 45 hours, and at 1400 and 1500 °C for 5 hours to observe the effects of increased duration and temperature on the reaction rate and mechanisms. For all durations at 1300 °C dendritic-like Ca₂RE₈(SiO₄)₆O₂ precipitates were formed within the residual CMAS melt. While a Ca₈MgRE(PO₄)₇ reaction layer was formed between the bulk pellets and residual CMAS which halted the penetration of CMAS into the bulk material. The thickness of the reaction layer increased with duration in a diffusion-controlled process that has a reaction rate comparable to those of single component rare earth phosphates. At 1400 °C, cristobalite recrystallizes within

the residual CMAS and there is a less dense and less uniform Ca₈MgRE(PO₄)₇ reaction layer at the pellet surface, with clear CMAS penetration into the bulk pellet. At 1500 °C, no reaction layer forms at the pellet surface, and the CMAS penetrates the entirety of bulk material via the grain boundaries. No large cracks or significant swelling occurred in the multicomponent phosphates which are typically observed in rare earth disilicates, further showing the improved CMAS corrosion resistance. Considering many possible combinations of rare earth elements to form the single phase xenotime structure, further work is still needed to optimize the multicomponent compositions, thermal properties, and corrosion resistance for EBC applications.

Declaration of Competing Interest

The authors declare that they have no conflict of interest.

Acknowledgment

This work was supported as part of the DMREF: Machine Learning Accelerated Design and Discovery of Rare-earth Phosphates as Next Generation Environmental Barrier Coatings. Standard Grant funded by the Division of Materials Research, National Science Foundation under Award DMREF-2119423.

References

- [1] N. P. Padture, "Advanced structural ceramics in aerospace propulsion," *Nature materials*, pp. 804-809, 2016.
- [2] J. L. Stokes, B. J. Harder, V. L. Wiesner and D. E. Wolfe, "High-Temperature thermochemical interactions of molten silicates with Yb2Si2O7 and Y2Si2O7

- environmental barrier coating materials," *Journal of the European Ceramic Society*, pp. 5059-5067, 2019.
- [3] J. H. Perepezko, "The hotter the engine, the better.," *Science*, pp. 1068-1069, 2009.
- [4] D. R. Clarke, M. Oechsner and N. P. Padture, "Thermal-barrier coatings for more efficient gas-turbine engines," *MRS bulletin*, vol. 37, no. 10, pp. 891-898, 2012.
- [5] L. R. Turcer, A. R. Krause, H. F. Garces, L. Zhang and N. P. Padture, "Environmental-barrier coating ceramics for resistance against attack by molten calcia-magnesia-aluminosilicate (CMAS) glass: Part I, YAlO3 and γ-Y2Si2O7," *Journal of the European Ceramic Society*, vol. 38, no. 11, pp. 3905-3913, 2018.
- [6] K. N. Lee, "Current status of environmental barrier coatings for Si-based ceramics," *Surface and Coatings Technology*, vol. 133, pp. 1-7, 2000.
- [7] L. R. Turcer, A. R. Krause, H. F. Garces, L. Zhang and N. P. Padture, "Environmental-barrier coating ceramics for resistance against attack by molten calcia-magnesia-aluminosilicate (CMAS) glass: Part II, β-Yb2Si2O7 and β-Sc2Si2O7," *Journal of the European Ceramic Society*, vol. 38, no. 11, pp. 3914-3924, 2018.
- [8] H. Zhao, B. T. Richards, C. G. Levi and H. N. Wadley, "Molten silicate reactions with plasma sprayed ytterbium silicate coatings," *Surface and Coatings Technology*, vol. 288, pp. 151-162, 2016.
- [9] J. Liu, L. Zhang, Q. Liu, L. Cheng and Y. Wang, "Calcium–magnesium–aluminosilicate corrosion behaviors of rare-earth disilicates at 1400° C," *Journal of the European Ceramic Society*, vol. 33, no. 15-16, pp. 3419-3428, 2013.
- [10] F. Stolzenburg, M. Johnson, K. N. Lee, N. S. Jacobson and K. T. Faber, "The interaction of calcium–magnesium–aluminosilicate with ytterbium silicate environmental barrier materials," *Surface and Coatings Technology*, vol. 284, pp. 44-50, 2015.

- [11] L. R. Turcer, "Next-Generation Thermal/Environmental Barrier Coatings for Ceramic-Matrix Composites," *Doctoral dissertation, Brown University*, 2020.
- [12] J. L. Smialek, "The chemistry of Saudi Arabian sand: a deposition problem on helicopter turbine airfoils," in *In Gordon Conference on Corrosion*, Cleveland, OH, United States, 1991.
- [13] R. I. Webster, N. P. Bansal, J. A. Salem, E. J. Opila and V. L. Wiesner, "Characterization of thermochemical and thermomechanical properties of Eyjafjallajökull volcanic ash glass," *Coatings*, vol. 10, no. 2, 2020.
- [14] C. G. Levi, J. W. Hutchinson, M.-H. Vidal-Sétif and C. A. Johnson, "Environmental degradation of thermal-barrier coatings by molten deposits," *MRS bulletin*, vol. 37, no. 10, pp. 932-941, 2012.
- [15] V. L. Wiesner, D. Scales, N. S. Johnson, B. J. Harder, A. Garg and N. P. Bansal, "Calcium–magnesium aluminosilicate (CMAS) interactions with ytterbium silicate environmental barrier coating material at elevated temperatures," *Ceramics International*, vol. 46, no. 10, pp. 16733-16742, 2020.
- [16] K. M. Grant, . S. Krämer, G. G. Seward and C. G. Levi, "Calcium–magnesium alumino-silicate interaction with yttrium monosilicate environmental barrier coatings," *Journal of the American Ceramic Society*, vol. 93, no. 10, pp. 3504-3511, 2010.
- [17] J. Han, Y. Wang, R. Liu and F. Wan, "Theoretical and experimental investigation of Xenotime-type rare earth phosphate REPO4,(RE= Lu, Yb, Er, Y and Sc) for potential environmental barrier coating applications," *Scientific Reports*, vol. 10, no. 1, pp. 1-13, 2020.
- [18] X. Hu, F. Xu, K. Li, Y. Zhang, Y. Xu and X. Zhao, "Thermal properties and Calcium-Magnesium-Alumina-Silicate (CMAS) resistance of LuPO4 as environmental barrier coatings," *Journal of the European Ceramic Society*, vol. 40, no. 4, pp. 1471-1477, 2020.

- [19] M. Ridley, B. McFarland, C. Miller and E. Opila, "YbPO4: A novel environmental barrier coating candidate with superior thermochemical stability," *Materialia*, vol. 21, p. 101289, 2022.
- [20] B. Ye, T. Wen, M. C. Nguyen, L. Hao, C.-Z. Wang and Y. Chu, "First-principles study, fabrication, and characterization of (Zr0.25Nb0.25Ti0.25V0.25)C high-entropy ceramics," *Acta Materialia*, vol. 170, pp. 15-23, 2019.
- [21] P. Sarker, T. Harrington, C. Toher, C. Oses, M. Samiee, J.-P. Maria, D. W. Brenner, K. S. Vecchio and S. Curtarolo, "High-entropy high-hardness metal carbides discovered by entropy descriptors," *Nature communications*, vol. 9, no. 1, pp. 1-10, 2018.
- [22] C. Ng, S. Guo, J. Luan, S. Shi and C. T. Liu, "Entropy-driven phase stability and slow diffusion kinetics in an Al0.5CoCrCuFeNi high entropy alloy," *Intermetallics*, vol. 31, pp. 165-172, 2012.
- [23] A. J. Wright, Q. Wang, S.-T. Ko, K. M. Chung, R. Chen and J. Luo, "Size disorder as a descriptor for predicting reduced thermal conductivity in medium- and high-entropy pyrochlore oxides," *Scripta Materialia*, vol. 181, pp. 76-81, 2020.
- [24] C. M. Rost, E. Sachet, T. Borman, A. Moballegh, E. C. Dickey, D. Hou, J. L. Jones, S. Curtarolo and J.-P. Maria, "Entropy-stabilized oxides," *Nature communications*, vol. 6, no. 1, pp. 1-8, 2015.
- [25] Y. Tan, C. Chen, S. Li, X. Han, J. Xue, T. Liu, X. Zhou and H. Zhang, "Oxidation behaviors of high-entropy transition metal carbides in 1200 °C water vapor," *Journal of Alloys and Compounds*, vol. 816, p. 152523, 2020.
- [26] Y. Dong, K. Ren, Y. Lu, Q. Wang, J. Liu and Y. Wang, "High-entropy environmental barrier coating for the ceramic matrix composites," *Journal of the European Ceramic Society*, vol. 39, no. 7, pp. 2574-2579, 2019.

- [27] G. E. Nikiforova, M. A. Ryumin, K. S. Gavrichev and V. M. Gurevich, "High-temperature thermodynamic properties of LuPO4," *Inorganic Materials*, vol. 48, no. 8, pp. 841-844, 2012.
- [28] K. S. Gavrichev, M. A. Ryumin, A. V. Tyurin, V. M. Gurevich, G. E. Nikiforova and L. N. Komissarova, "Heat capacity and thermodynamic functions of YbPO4 from 0 to 1800 K," *Inorganic Materials*, vol. 49, no. 7, pp. 701-708, 2013.
- [29] K. S. Gavrichev, M. A. Ryumin, A. V. Tyurin, V. M. Gurevich, A. V. Khoroshilov and L. N. Komissarova, "Thermodynamic functions of erbium orthophosphate ErPO4 in the temperature range of 0–1600K," *Thermochimica acta*, vol. 535, pp. 1-7, 2012.
- [30] K. S. Gavrichev, M. A. Ryumin, A. V. Tyurin, V. M. Gurevich and L. N. Komissarova, "Heat Capacity and Thermodynamic Functions of Xenotime YPO4(c) at 0-1600 K," *Geochemistry International*, vol. 48, no. 9, pp. 932-939, 2010.
- [31] V. M. Gurevich, M. A. Ryumin, A. V. Tyurin and L. N. Komissarova, "Heat capacity and thermodynamic properties of GdPO4 in the temperature range 0–1600 K," *Geochemistry International*, vol. 50, no. 8, pp. 702-710, 2012.
- [32] A. Aygun, A. L. Vasiliev, N. P. Padture and X. Ma, "Novel thermal barrier coatings that are resistant to high-temperature attack by glassy deposits," *Acta Materialia*, vol. 55, no. 20, pp. 6734-6745, 2007.
- [33] M. Winter, "The periodic table of the elements by WebElements," 17 July 2022. [Online]. Available: https://www.webelements.com/.
- [34] K. Yang, K. Bryce, W. Zhu, D. Zhao and J. Lian, "Multicomponent pyrochlore solid solutions with uranium incorporation A new perspective of materials design for nuclear applications," *Journal of the European Ceramic Society*, vol. 41, no. 4, pp. 2870-2882, 2021.

- [35] M. Tong, Y. Liang, G. Li, Z. Xia, M. Zhang, F. Yang and Q. Wang, "Luminescent properties of single Dy3+ ions activated Ca3Gd7(PO4)(SiO4)5O2 phosphor," *Optical materials*, vol. 36, no. 9, pp. 1566-1570, 2014.
- [36] F. Wang, L. Guo, C. Wang and F. Ye, "Calcium-magnesium-alumina-silicate (CMAS) resistance characteristics of LnPO4 (Ln=Nd, Sm, Gd) thermal barrier oxides," *ournal of the European Ceramic Society*, vol. 37, no. 1, pp. 289-296, 2017.
- [37] R. I. Webster and E. J. Opila, "Viscosity of CaO-MgO-Al2O3-SiO2 (CMAS) melts: Experimental measurements and comparison to model calculations," *Journal of Non-Crystalline Solids*, vol. 584, p. 121508, 2022.
- [38] F. Shimizu, H. Tokunaga, N. Saito and K. Nakashima, "Viscosity and surface tension measurements of RE2O3–MgO–SiO2 (RE=Y, Gd, Nd, and La) melts," *ISIJ international*, vol. 46, no. 3, pp. 388-393, 2006.
- [39] J. L. Stokes, B. J. Harder, V. L. Wiesner and D. E. Wolfe, "Effects of crystal structure and cation size on molten silicate reactivity with environmental barrier coating materials," *Journal of the American Ceramic Society*, vol. 103, no. 1, pp. 622-634, 2020.
- [40] J. L. Stokes, B. J. Harder, V. L. Wiesner and D. E. Wolfe, Melting and Crystallization Behavior of CaO-MgO-Al2O3-SiO2 Silicates Relevant to Turbine Engine Applications, NASA Technical Reports Server E-19974, 2021.
- [41] I. Mazilin, N. Zaitsev, L. Baldaev, E. Marchukov and D. Drobot, "Effect of neodymia, samaria and yttria co-doping on the phase stability, thermal conductivity and long-term performance of the zirconia-based thermal barrier coatings," in *International Thermal Spray Conference (ITSC)*, Shanghai, PRC, 2016.
- [42] A. G. Evans and J. W. Hutchinson, "The mechanics of coating delamination in thermal gradients," *Surface and Coatings Technology*, vol. 201, no. 18, pp. 7905-7916, 2007.

- [43] Y. Tan, C. Chen, S. Li, X. Han, J. Xue, T. Liu, X. Zhou and H. Zhang, "Oxidation behaviors of high-entropy transition metal carbides in 1200 °C water vapor," *Journal of Alloys and Compounds*, vol. 816, p. 152523, 2020.
- [44] Y. Dong, K. Ren, Y. Lu, Q. Wang, J. Liu and Y. Wang, "High-entropy environmental barrier coating for the ceramic matrix composites," *Journal of the European Ceramic Society*, vol. 39, no. 7, pp. 2574-2579, 2019.
- [45] X. Wang, M. Cheng, G. Xiao, C. Wang, R. Qiao, F. Zhang, Y. Bai, Y. Li, Y. Wu and Z. Wang, "Preparation and corrosion resistance of high-entropy disilicate (Y0.25Yb0.25Er0.25Sc0.25)2Si2O7 ceramics," *Corrosion Science*, vol. 192, p. 109786, 2021.
- [46] L. Sun, Y. Luo, Z. Tian, T. Du, X. Ren, J. Li, W. Hu, J. Zhang and J. Wang, "High-temperature corrosion of (Er0.25Tm0.25Yb0.25Lu0.25)2Si2O7 environmental barrier coating material subjected to water vapor and molten calcium–magnesium–aluminosilicate (CMAS)," *Corrosion Science*, vol. 175, p. 108881, 2020.